Effect of Roughness on Transition on the BOLT-1a Geometry in Supersonic Flow

Jonathan Davami* and Thomas J. Juliano†
University of Notre Dame, Notre Dame, Indiana, 46556, USA

Amanda Chou‡ and Andrew Leidy §
NASA Langley Research Center, Hampton, Virginia, 23681, USA

Infrared thermography measurements on an 8.8% scale BOLT-1a model were made in the NASA Langley Probe Calibration Tunnel for freestream unit Reynolds numbers from 7.7×10^6 /m to 30.7×10^6 /m, a freestream Mach number of 3.5, and nominal angle of attack of 0 degrees. The model was printed from polycarbonate and tested before and after fine-grit sanding to evaluate the effect of surface roughness on transition. Global surface roughness measurements were obtained using a 3D optical profilometer. The temperature distributions on the upper and lower experimental surfaces of the test article were simultaneously captured using two infrared cameras. Prior to testing, the facility freestream environment was characterized. At a freestream unit Reynolds number of approximately 17×10^6 /m, the nozzle-wall boundary layer began to transition nonuniformly, inducing transition on the model. The boundary-layer state was determined by analyzing Stanton number distributions computed from the surface temperature measurements. The present supersonic conditions that were examined on BOLT-1a were found to display both similarities and disparities in comparison to previous hypersonic experiments.

Nomenclature

c_p	Specific Heat at Constant Pressure, J/(kg · K)	α	Thermal Diffusivity, mm^2/s
f	Frequency, Hz	ϵ	Emissivity
k	Thermal Conductivity, W/(m · K)	κ	Wavenumber, /mm
L	Model Length	ρ	Density, kg/m^3
M	Mach Number	λ	Wavelength, mm
N	N Factor		
p	Pressure, Pa	*Subscripts*	
$\dot{q''}$	Heat Flux, W/m^2	0	Stagnation Conditions
Re	Reynolds Number	∞	Freestream Conditions
St	Modified Stanton Number	wall	Model Surface
T	Temperature, K	L	Model Length
x	Streamwise Distance, m		
y	Spanwise Distance, m		

I. Introduction

Aerodynamic heating due to boundary-layer transition is a major concern for hypersonic vehicle designers. Although laminar boundary layers generate relatively low levels of skin friction and surface heating, they tend to separate more easily than their turbulent counterparts. On the other hand, turbulent boundary-layers possess a smaller shape factor and greater momentum, resulting in reduced separation tendencies, but leading to elevated surface heating through an increase in skin friction. In scenarios where the boundary layer remains attached, the heat flux undergoes a significant

*Graduate Student, Aerospace and Mechanical Engineering Department, Student Member, AIAA.
†Associate Professor, Department of Aerospace and Mechanical Engineering. Associate Fellow, AIAA.
‡Research Aerospace Engineer, Flow Physics & Control Branch, M/S 170, AIAA Senior Member.
§Research Aerospace Engineer, Flow Physics & Control Branch, M/S 170, AIAA Member.

spike during transition, and since the extent of the overshoot cannot be accurately predicted, the design of thermal protection systems is highly dependent on the altitude at which boundary-layer transition occurs. Transition has been documented to cause surface heating rates to surge by a factor ranging from 3 to 8 [1–3]. The ability to control transition is of great interest, as it offers a potential means of regulating both viscous drag and surface heating distributions.

Boundary-layer transition in compressible flows is often challenging to predict since there are many contributing factors that occur simultaneously [4]. Furthermore, the pathway to transition is dependent on the state of the forcing environment [5]. Typically, transition initiates from forced disturbances that occur near the leading edge of the geometry. Disturbances resulting from interactions between freestream turbulence, noise, and small surface roughness elements excite the laminar boundary layer eigenmodes, a process known as receptivity. The growth of these instabilities is described by the linearized, unsteady Navier–Stokes equations. Disturbance growth can become nonlinear and lead to secondary instabilities in the form of mean flow distortions [6]. From here, the path to turbulence progresses rapidly through nonlinear interactions [4, 5, 7, 8].

The BOundary Layer Transition Flight Experiment (BOLT) was designed to evaluate the ability of modern simulations and ground experiments to understand and predict transition during hypersonic flight, using a new complex geometry that results in a 3D flowfield [9]. Computational studies using a relatively new quiet Direct Numerical Simulation (DNS) approach have revealed that the BOLT configuration exhibits four different instability mechanisms under hypersonic flow [10]. These mechanisms are a vortical mode situated close to the centerline, a traveling crossflow mode along the leading edge, as well as second-mode and mixed modes in the inboard region. Experiments on a 33% scaled BOLT model with fast-response surface-pressure transducers, hot-wire anemometry, and Infrared (IR) thermography were performed in both quiet and conventional-noise conditions [11]. They revealed transition fronts caused by two mechanisms in the latter case: one at the mixed-mode interaction region and a less prominent one in the outboard region where the traveling crossflow instability is present.

Previous wind-tunnel tests on the BOLT configuration have been done at hypersonic speeds ($M > 5$); however, the BOLT flight test did not reach the intended flight conditions ($M = 5$–7) [12]. The flight test gathered data at supersonic speeds ($M = 2$–4). Therefore, these post-flight ground tests were carried out at as-flown Mach numbers to discern significant disparities and similarities with flight data as well as with data from the many hypersonic ground tests.

II. Model and Facility

A. Model

The BOLT-1a configuration is a hyperbolic cone with side gutters [9]. The ground-test article was scaled by 8.8% of the flight-test vehicle to fit in the test core of the facility, with the nose positioned at the nozzle exit plane (Fig. 1). The model was printed using a stereolithography 3D printer with a 250 mW laser capable of printing layer sizes ranging from 25–300 μm, a XY resolution of 25 μm, and an 85 μm laser spot size. The model was made of polycarbonate, with the printing process starting at the base and ending at the nose tip. After printing, a stainless steel sting was fitted into the model [13].

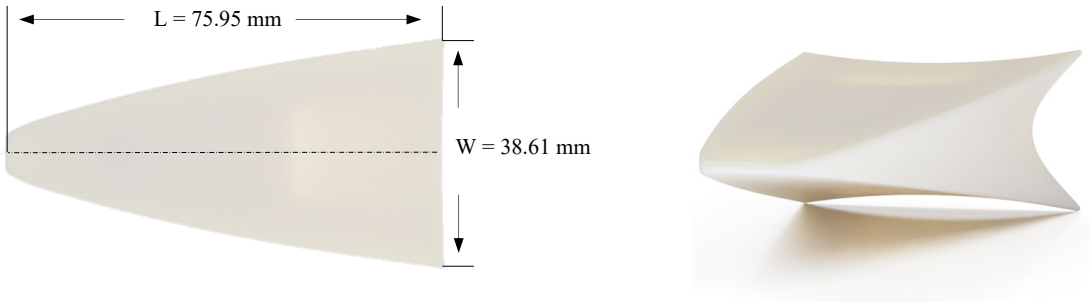
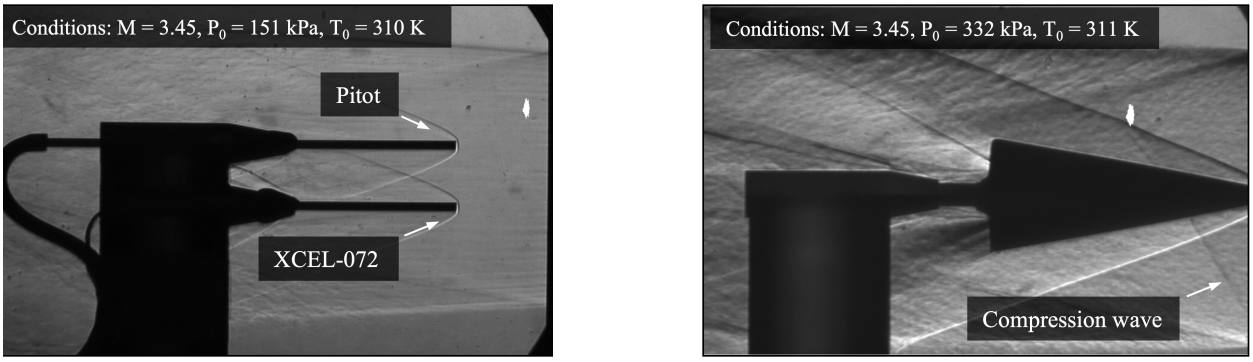


Fig. 1 8.8% scale BOLT-1a model.

B. Facility

The experiment was conducted in the NASA Langley Probe Calibration Tunnel (PCT), an open-jet tunnel with interchangeable axisymmetric nozzles. The tunnel is a risk-reduction facility used for initial experimental setups and calibration of instrumentation. Since it can operate continuously for a long period of time (more than 2 hours) due to low mass flow and large bottle fields and vacuum spheres, it is an appealing choice for testing at numerous freestream unit Reynolds numbers.

The PCT was equipped with a nominal Mach 3.5 nozzle. The diameter of the nozzle exit is 76.2 mm. The PCT freestream flow was characterized using an XCEL-072-25A Kulite® and a pitot probe (Fig. 2a) plumbed to a Mensor. Both probes were instrumented on a double-sting holder bolted on a spanwise traversing stage approximately 2.54 cm away from the nozzle exit plane with respect to the sensor tips. The sensors were centered across the nozzle centerline vertically and were traversed in the spanwise direction.

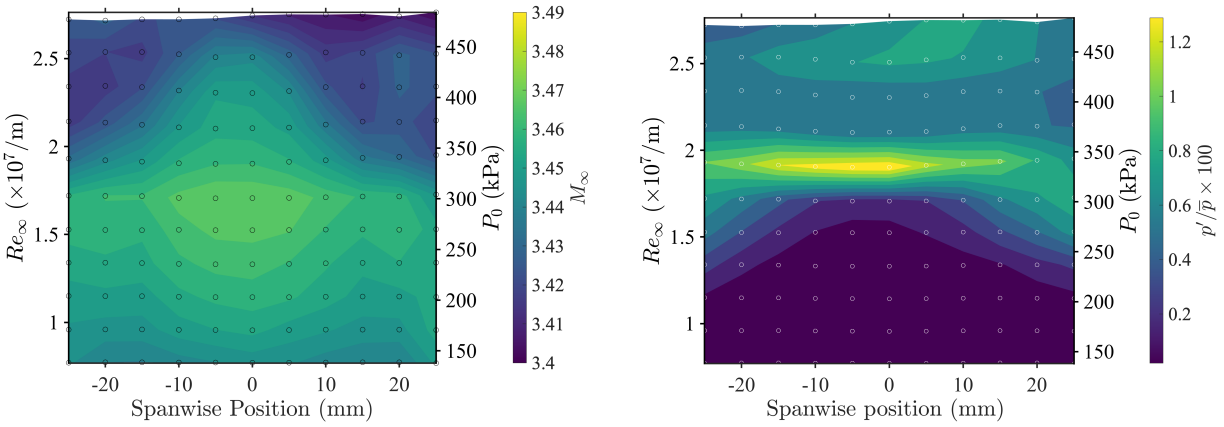


(a) Kulite and Pitot probe. **(b) BOLT-1a scale model.**

Fig. 2 Schlieren images [Source: NASA].

Figure 3a shows a contours of Mach number as a function of freestream unit Reynolds number and spanwise position. The nozzle centerline is $y = 0$. The Mach number was computed using the Rayleigh-Pitot equation with pitot probe data. Figure 3b shows contours of freestream noise measured by the Kulite® as a function of stagnation pressure and spanwise position. The root-mean-square (RMS) pressure fluctuation levels shown in Fig. 4 were determined by computing the square root of the integrated power spectral densities. The RMS amplitudes were calculated for a frequency bandwidth ranging from 500 Hz to 50 kHz to exclude the Kulite® resonance and are shown as a percentage of the Kulite® mean pressure. The centerline freestream noise level increases from 0.2% to 1.4% between freestream unit Reynolds numbers of 17×10^6 /m and 20×10^6 /m. This significant rise in freestream noise indicates that the nozzle-wall boundary layer is undergoing transition. For $Re_\infty > 20 \times 10^6$ /m, the freestream noise decreases from its peak during transition, but is still much higher than at lower Re_∞, indicating a turbulent nozzle-wall boundary layer.

Subsequent hot-wire and schlieren measurements (not shown) indicated that the nozzle-wall boundary-layer transition was not axisymmetric. The lower and upper portions transitioned at $Re_\infty \approx 17 \times 10^6$ /m and $\approx 23 \times 10^6$ /m, respectively. Schlieren images at $Re_\infty \approx 17 \times 10^6$ /m show occasional compression waves from the lower nozzle wall believed to be caused by turbulent bursts (Fig. 2b). The wave angles were roughly 60°, much larger than the Mach angle of 17° for this M_∞. The specific origin of these intermittent waves is not known, but their weak interaction with the bow shock suggests that they may impact the measurements. At $Re_\infty \approx 23 \times 10^6$ /m, compression waves were emitted from the upper portion of the nozzle.



(a) Mach number (Pitot probe). **(b) Noise level (Kulite).**

Fig. 3 Freestream characterization.

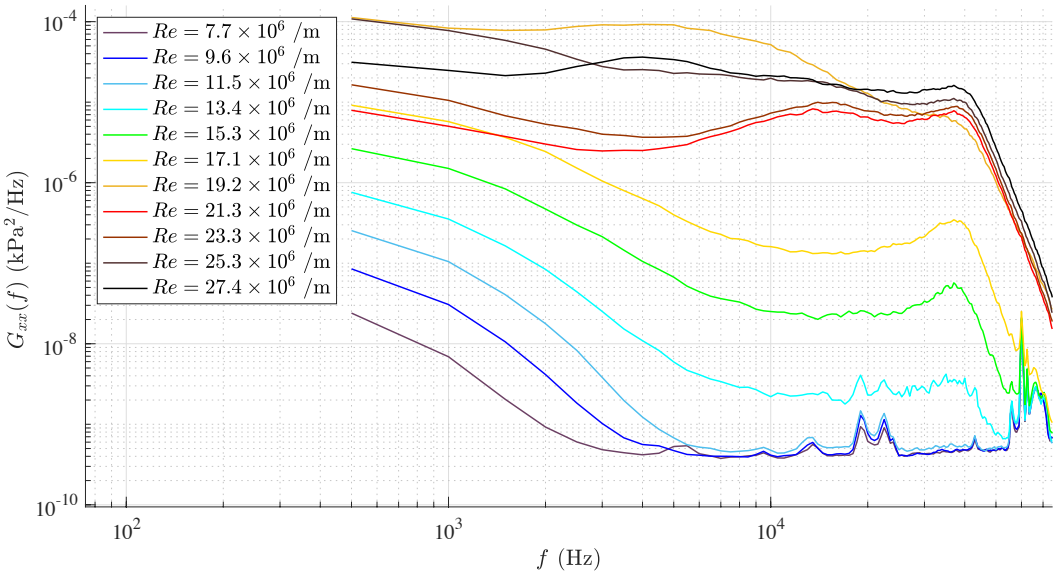


Fig. 4 Centerline autospectral densities.

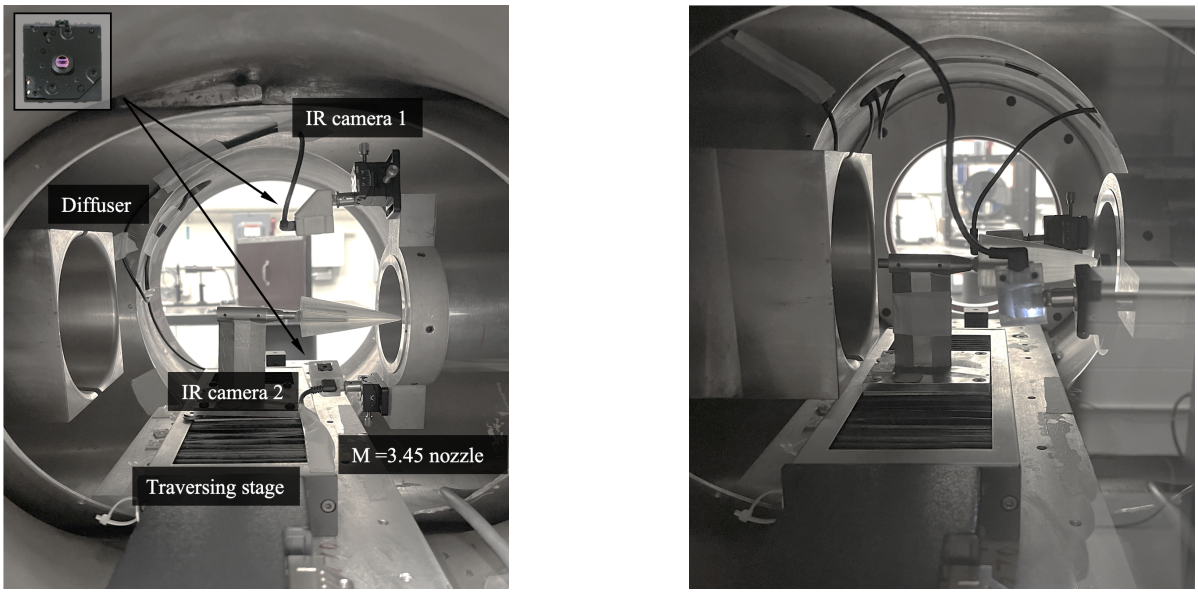
III. Experimental Setup & Instrumentation

Infrared (IR) thermography and schlieren images were acquired to document the boundary layer state on the model. Figure 5 shows the experimental setup. Two IR cameras were used to simultaneously measure the model upper and lower surfaces. The cameras were mounted inside the test section on a collar bolted around the nozzle. Both the collar and the models were rolled by 90 degrees once the surface of the model was sanded (Fig. 5b).

A. Infrared Thermography

The model surface temperature was measured with two identical long-wave infrared (8–14 μm wavelength) cameras. Their spatial resolution is 160×120 pixels with a maximum frame rate of 8.7 fps. Prior to testing, both cameras were calibrated with a black body calibration source indicating that the measured temperatures agreed well with the existing factory calibration. The overall uncertainty of the IR camera temperature measurement is ±5 K. The thermal properties of the polycarbonate are listed in Table 1. The emissivity of the polycarbonate was assumed to be $\epsilon = 0.94$ [14, 15].

To plot the surface temperatures in Cartesian coordinates, a perspective transformation matrix was calculated.



(a) Unsanded model. **(b) Sanded model.**

Fig. 5 Experimental setup in the PCT [Source: NASA].

Table 1 Thermal properties of polycarbonate [13].

c_p	α	ρ	k	ϵ
2880 J/(kg · K)	0.0990 mm^2/s	993 kg/m^3	0.283 W/(m · K)	0.94

The viewing angles were determined based on the camera and model relative positions, and a directional emissivity correction was applied. Heat flux was then calculated by solving the transient 1D heat equation using the `FORTRAN` QCALC subroutine translated to MATLAB [16]. The code assumes one-dimensional heat transfer normal to the surface and uses a second-order Euler explicit finite difference approximation to solve for the temperature distribution through the wall; heat flux is obtained from a second-order approximation to the derivative of the temperature profile at the outer surface [17]. The initial condition was based on the prerun thermographs, with the assumption of a uniform surface temperature distribution. An adiabatic boundary condition was assumed at the centerplane of the model.

The Stanton number was computed to nondimensionalize the heat flux. Throughout this work, a modified Stanton number,

$$St = \frac{\dot{q''}\text{wall}}{c_p \rho_\infty u_\infty (T_0 - T_\text{wall})} \quad , \tag{1}$$

is used, where $\dot{q''}_\text{wall}$, c_p, ρ_∞, u_∞, T_0, and T_wall represent the heat flux, the heat capacity of air at constant pressure, freestream density, freestream velocity, stagnation temperature, and wall temperature, respectively. The freestream quantities were calculated using isentropic relations with the measured stagnation pressure, stagnation temperature, and Mach number from each run. A standard heat capacity of air at constant pressure, 1004 J/kg·K, was assumed. Uncertainty analysis of Eq. 1 yielded an uncertainty estimate for St of $+26/-19\%$. The ±5 K uncertainty in temperature is the largest contributor to this estimate.

This work employs two methods for visualizing the heating of the model, namely, global Stanton number distributions, $St(x/L, y/L)$, and streamwise profiles of Stanton number along the centerline, $St(x/L)$. The latter approach serves to characterize the boundary-layer state for each freestream unit Reynolds number condition. However, due to the unavailability of computational results, it is not possible to use the deviation from a predicted laminar heating rate as a criterion for detecting boundary-layer transition. Consequently, the heat-flux minimum of a given $St(x/L)$ is used to pinpoint transition locations.

IV. Test Conditions

Data were acquired at freestream unit Reynolds numbers from 7.7×10^6 /m to 26.9×10^6 /m for the as-printed model and 7.7×10^6 /m to 30.7×10^6 /m for the sanded model (Table 2). The models were kept in the flow from the tunnel startup through shutdown. Stagnation temperature was kept constant while stagnation pressure was stepped and held at each condition.

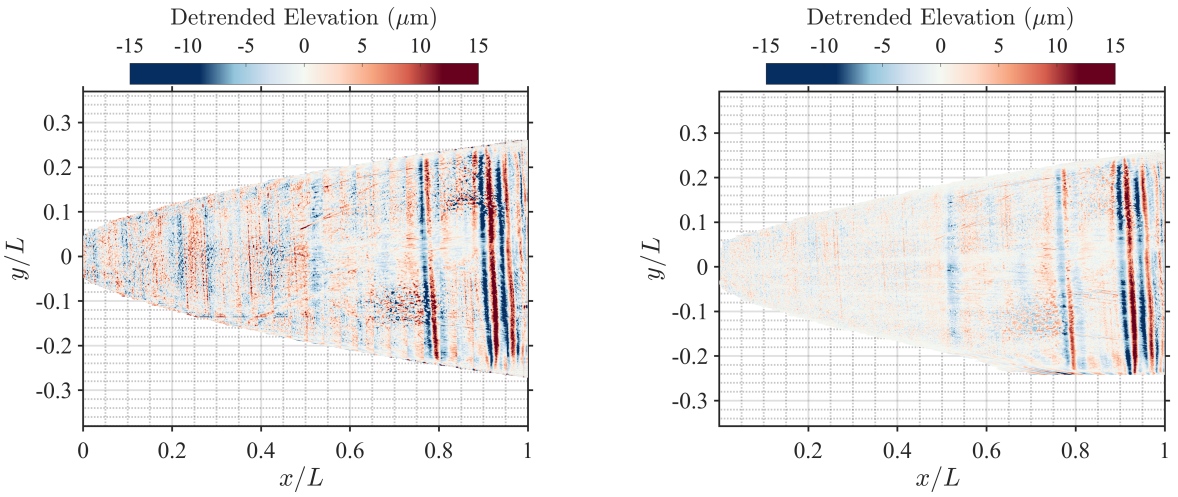
The upper and lower surface heating distributions were compared to align the model at nominally zero angle of attack. Shims were placed between the traverse stage and probe stand interface until a similar heating pattern was observed on both surfaces at a given Re_∞.

Table 2 Test conditions.

Condition	M_∞	P_0 (kPa)	T_0 (K)	Re_∞ ($\times 10^6$/m)	Re_L ($\times 10^6$)	$(p'/\overline{p})_{\text{centerline}}$
1	3.45	138	311	7.7 ± 0.1	0.6	0.02%
2	3.45	207	311	11.5 ± 0.1	0.9	0.04%
3	3.45	276	311	15.4 ± 0.1	1.2	0.10%
4	3.45	345	311	19.2 ± 0.1	1.5	1.44%
5	3.45	414	311	23.0 ± 0.1	1.8	0.60%
6	3.45	483	311	26.9 ± 0.1	2.0	0.38%
7	3.45	552	311	30.7 ± 0.2	2.3	–

V. Model Surface Conditions

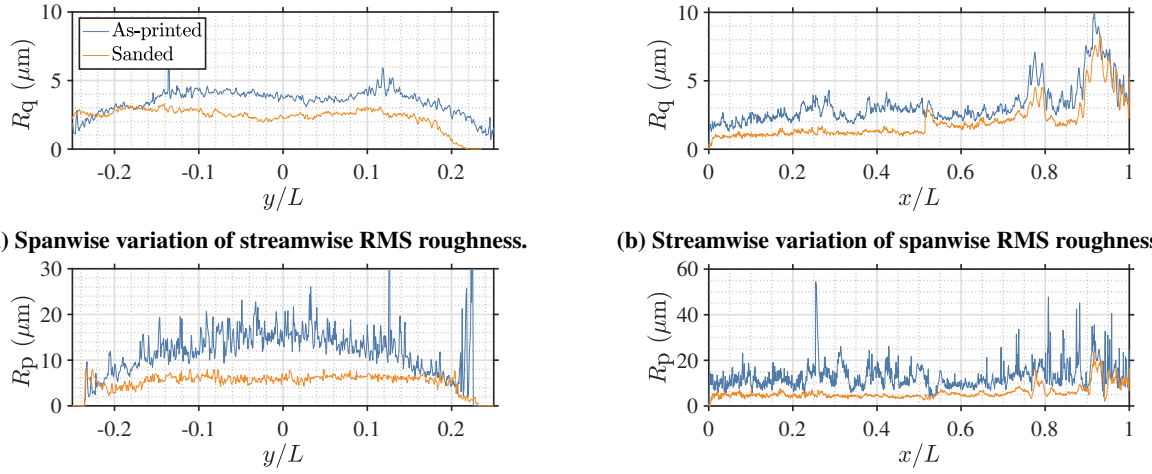
The upper and lower surfaces of the model were scanned using a 3D optical profilometer before testing. Once the baseline data set was obtained, the surfaces were sanded with 600 grit sandpaper and scanned again. Figure 7 presents surface plots of detrended elevation before and after sanding for side 1 of the model. The streamwise (x) and spanwise (y) coordinates are normalized by the length of the model (L). Spanwise striations are present in both roughness distributions, and their wavelength changes in the streamwise direction. This is most likely because the models were printed with an adaptive layer thickness setting, meaning that the thickness of each layer becomes finer as the printer nears the nose tip of the model. Small-wavelength roughness is visible in the as-printed distribution at $(x/L, y/L) \approx (0.7, -0.1)$ and $(x/L, y/L) \approx (0.9, 0.1)$, but it is obscured by the large wavelength spanwise striations.



(a) As-printed. **(b) Sanded.**

Fig. 6 Surface roughness distributions on side 1.

Figures 7a and 7b depict the spanwise variation of the streamwise root-mean-square (RMS) roughness and the streamwise variation of the spanwise RMS roughness for both the as-printed and sanded roughness distributions. The mean RMS roughness for each roughness distribution of side 1, as-printed and sanded, is 3.3 μm and 2.0 μm, respectively. Figures 7c and 7d display the spanwise variation of the largest streamwise peaks and the streamwise variation of the largest spanwise peaks. Note that the spanwise variation of the largest streamwise peaks was only computed from $x/L = 0$ to $x/L = 0.7$, as the striations near the base of the model have comparable magnitudes for both roughness distributions. The magnitude of the largest peaks in the streamwise direction is, on average, 2–4 times larger for the as-printed roughness distribution than for the sanded model. Previous studies on the effect of roughness on boundary layer instabilities suggest that the peak amplitude of roughness is the most dominant feature to consider; however, it is not sufficient to fully assess the impact of distributed roughness [18].



(a) Spanwise variation of streamwise RMS roughness.

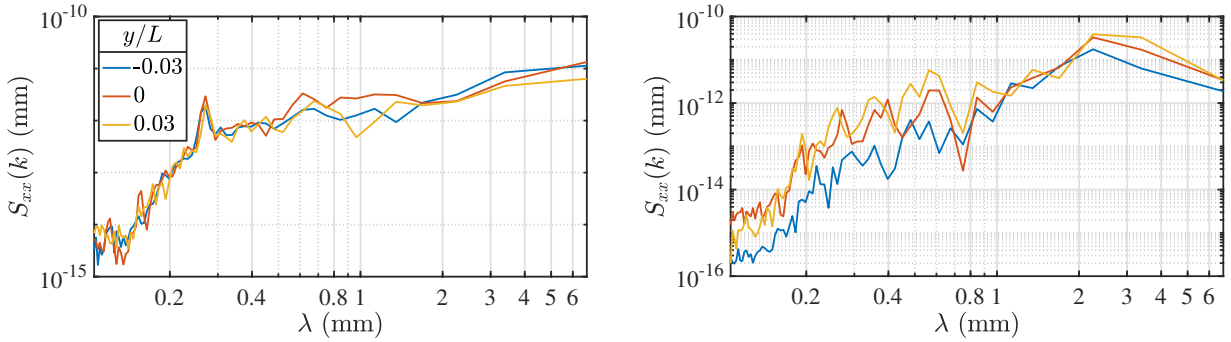
(b) Streamwise variation of spanwise RMS roughness.

(c) Spanwise variation of the largest streamwise peaks.

(d) Streamwise variation of the largest spanwise peaks.

Fig. 7 Comparison of as-printed to sanded roughness parameters on side 1.

To determine if the striations correspond to the thickness of a printed layer ($\approx$ 300 microns), the wavelength of the striations was characterized by computing auto spectral densities of streamwise roughness profiles. The auto spectral density is calculated for the as-printed roughness distribution from $x/L = 0$ to $x/L = 0.75$ (Fig. 8a) and from $x/L = 0.75$ to $x/L = 1$ (Fig. 8b) at various spanwise locations. In Fig. 8a, two prominent peaks corresponding to wavelengths of $\lambda = 0.27$ mm and $\lambda = 0.61$ mm are observed, while Fig. 8b displays high energy at $\lambda = 2.2$ mm, accompanied by peaks at $\lambda = 0.61$ mm, $\lambda = 0.35$ mm, and $\lambda = 0.27$ mm. Notably, the peak at $\lambda = 0.27$ m appears less pronounced in Fig. 8b than in Fig. 8a.



(a) From $x/L = 0$ to $x/L = 0.75$.

(b) From $x/L = 0.75$ to $x/L = 1$.

Fig. 8 Autospectral densities of streamwise detrended elevation at various span locations for as-printed roughness on side 1.

While Fourier analysis may be useful for studying the spectral dynamics of surface roughness, it does not provide

information about the local spatial variation of wavenumber. To track the streamwise evolution of the spatial frequencies, the Morlet wavelet transformation is employed on the detrended elevation across $y/L = 0$ for the as-printed roughness. The wavelet analysis enables the observation of the evolution of localized events over time and is often presented in event-duration–time space [19]. In this analysis, the results are presented in wavelength–normalized streamwise coordinate space.

Figure 9 shows a surface plot of wavelet coefficients in wavelength–normalized streamwise coordinate space. The wavelet transformation is quasilocal in both physical space and Fourier space, allowing for the analysis of the local wavelength evolution across the model. Starting from the nose tip, wavelengths of $\lambda = 0.27$ mm and $\lambda = 0.61$ mm are dominant up to $x/L \approx 0.74$. A wavelength of $\lambda = 0.27$ mm corresponds well with the standard thickness layer of the printer (0.3 mm). Farther downstream, the dominant wavelength increases significantly to 2.1 mm, which corresponds to the larger striations previously identified. This wavelength is significantly larger than the printer's standard layer thickness. They may result from a defect in 3D prints known as "bleeding/elephant's foot," which occurs when the weight of the print pushes down on a weak or incompletely cured lower layer. Even after sanding the model, these striations remain visible.

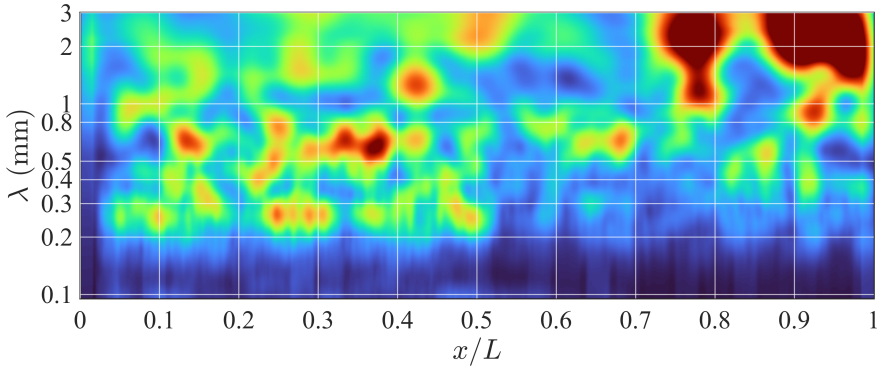


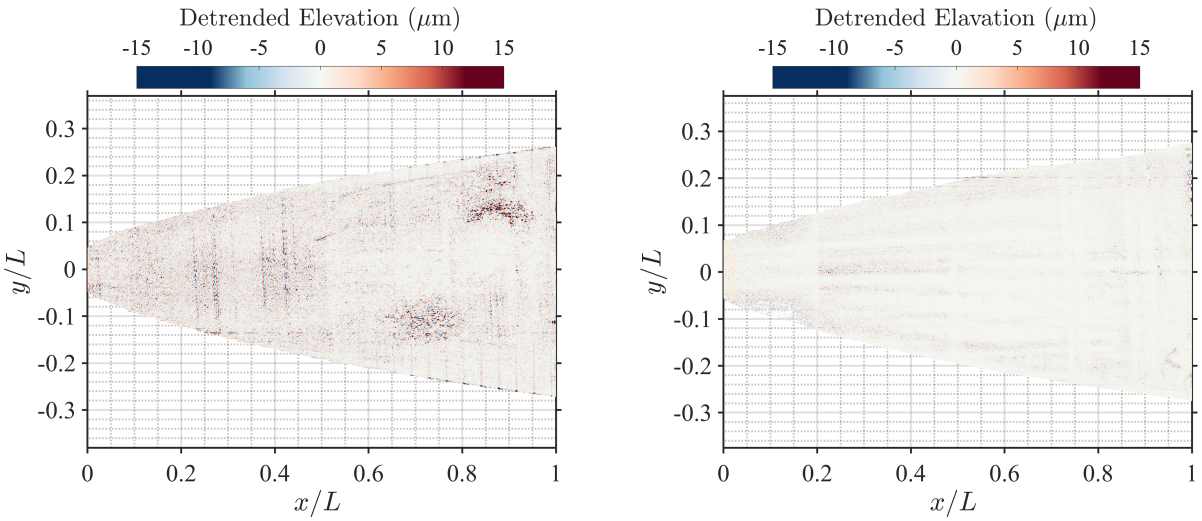
Fig. 9 Morlet wavelet transformation in wavelength–normalized streamwise coordinate space.

To better visualize short wavelength roughness, the dominant wavelengths of the striations were filtered out. First, a 2D Fourier transformation was computed for the roughness distributions shown in Fig. 7, and a cutoff spatial frequency of $\kappa = 3.7$ /mm (corresponding to $\lambda = 0.27$ mm) was applied. Fourier coefficients with magnitudes below this value were set to zero, resulting in filtered Fourier coefficients. Next, the filtered coefficients were subjected to a 2D inverse Fourier transformation to obtain the filtered surface roughness data. This process was performed for both the as-printed and sanded roughness distributions, and the results are shown in Fig. 10. Patches of small-wavelength roughness on the as-printed model were significantly reduced by sanding.

The roughness distribution of side 2 was analyzed using the same methods as for side 1. However, there are three notable differences between the sanded distributions. Side 2 was sanded in a circular motion, which is visible in the roughness distribution (not shown). This difference was found to not visibly impact the surface heating. Second, when filtering the high-wavelength roughness distribution for side 2, it was discovered that the largest amplitude roughness was located at the base of the model for the as-printed roughness distribution, which are remnants of the print supports. Unlike side 1, there is almost no high-wavelength roughness present on side 2 of the model. Finally, there is a small area of noticeably higher roughness on the centerline of side 2 in the as-printed roughness distribution. However, this roughness is considered nonphysical as it resulted from a glare of light reflecting off the metal sting through the polycarbonate and into the optical profilometer. Consequently, this section has been removed from the as-printed roughness distribution of side 2. The removed section can be observed in Fig. 14, particularly between $x/L = 0.5$ and 1.

Table 3 summarizes the roughness characteristics of both sides of the model for the as-printed and sanded roughness distributions. $\overline{R_a}$ is the arithmetic mean of the absolute values of the deviations of the roughness from the mean and represents the average roughness of the surface. $\overline{R_q}$ is the root mean square of the deviations from the mean and is more sensitive to small-scale variations than $\overline{R_a}$. After sanding, $\overline{R_a}$ and $\overline{R_q}$ for both sides are reduced by approximately 35%. For both sides, $\overline{R_q}$ is smaller than $\overline{R_a}$ before and after sanding, indicating the roughness has more high-amplitude peaks and valleys, but few fine-scale variations. This may indicate that the sanding process removed larger roughness features,

but still containing some larger irregularities. $\overline{R_p}$ and $\overline{R_v}$ represent the mean of the largest peaks and valleys over the roughness distributions. The ratios of $\overline{R_p}/\overline{R_v}$ before and after sanding are 1.33 and 0.90 for side 1 and for side 2 are 1.33 and 1.04. These suggest that the surface is smoother overall, with peaks and valleys of similar magnitudes. The mean skewness is $\overline{R_{sk}}$ and represents the degree of asymmetry of the roughness profile about its mean. The sign change in skewness from sanding indicates that there are now more valleys than peaks. By sanding the surface, scratches were most likely introduced. The kurtosis, $\overline{R_{kur}}$, represents the sharpness of the peaks of the roughness. The observed decrease in kurtosis implies that sanding reduced the quantity of sharp peaks and valleys.



(a) As-printed. **(b) Sanded.**

Fig. 10 Filtered surface roughness distributions on side 1.

Table 3 Summary of roughness characteristics.

	Side 1 as-printed	Side 1 sanded	Side 2 as-printed	Side 2 sanded
$\overline{R_a}$ (μm)	2.1	1.4	1.9	1.2
$\overline{R_q}$ (μm)	3.3	2.0	2.9	1.9
$\overline{R_p}$ (μm)	10.0	3.7	9.3	5.4
$\overline{R_v}$ (μm)	7.5	4.1	7	5.2
$\overline{R_{sk}}$	-0.03	0.17	-0.01	0.20
$\overline{R_{kur}}$	6.6	2.4	6.6	2.3

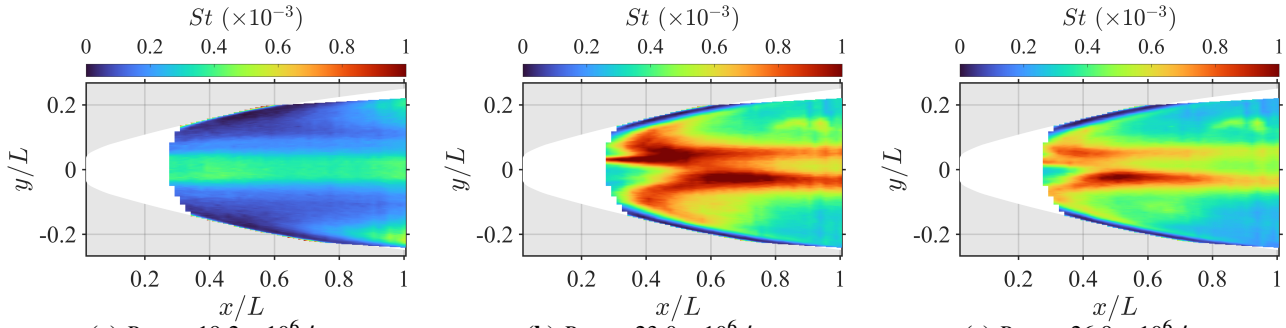
VI. Experimental Results

A. Thermography of As-Printed Surface Roughness

The IR thermography results are independently presented for both the as-printed and sanded roughness distributions, followed by a comparative analysis. Figures 11 and 12 show St distributions on sides 1 and 2 of the as-printed roughness distribution for $Re_\infty = 19.2 \times 10^6$ /m, 23.0×10^6 /m, and 26.9×10^6 /m. In this experiment, side 1 was the lower surface and side 2 is the upper (refer to Fig. 5a). Due to the positioning and limited field of view of the IR cameras, data collection near the nose of the model was restricted. It is anticipated that the transition behavior on side 1 will undergo a significant change at $Re_\infty \approx 17 \times 10^6$ /m as the nearby nozzle wall undergoes transition, and that side 2 will exhibit similar transformation at $Re_\infty \approx 23 \times 10^6$ /m.

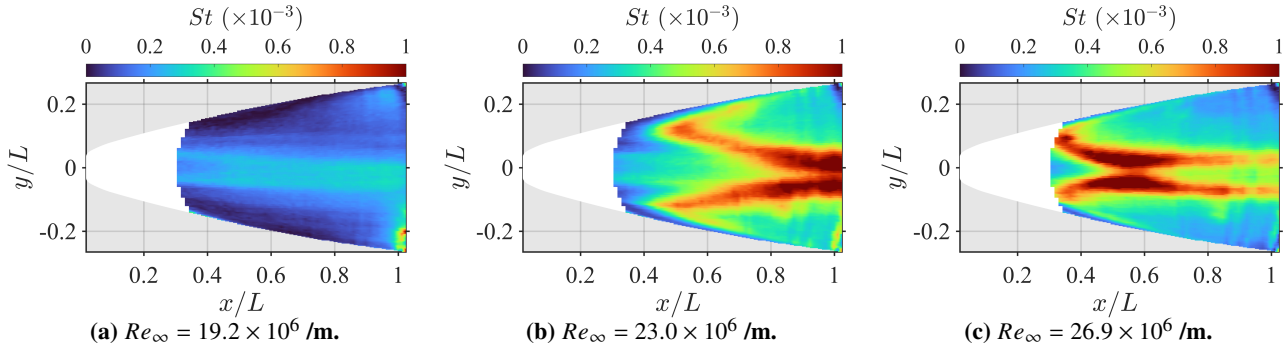
At $Re_\infty = 19.2 \times 10^6$ /m, St is high across the centerline and at the corner outboard regions for both sides of the model. Prior experimental studies on the BOLT-1a in hypersonic flow consistently show that the outboard regions of the geometry experience higher levels of heating compared to the centerline [20, 21]. In hypersonic flow, increases in Re_∞ tend to have a greater impact on the outboard regions as compared to the centerline, which remains relatively resistant even after boundary-layer transition has occurred in the outboard regions. This is attributed to the fact that the boundary layer on the centerline is thicker than that on the outboard regions, where the highly swept leading edges induce crossflow and result in boundary-layer transition occurring at a lower Re_∞ than on the centerline. However, in the present experiment, higher heating is observed on the centerline. Note that the freestream noise level was higher on side 1 at this Re_∞, resulting in a higher St. While hot streaks are visible near the centerline, they are faint. Previous experiments have shown these structures are less prominent in conventional-noise flows [22].

Increasing Re_∞ to 23.0×10^6 /m leads to the formation of transition lobes on either side of the centerline, with the maximum heating concentrated along the inner regions of each respective lobe. However, in hypersonic flow, the maximum heating is found on the outboard regions of each lobe rather than the center regions [20]. The streamwise location of the lobes on each side of the model are not equivalent since the upper and lower portions of the nozzle transition at different Re_∞ and induces a nonaxisymmetric freestream noise environment onto the model (only from $Re_\infty \approx 17 \times 10^6$ /m to $\approx 23 \times 10^6$ /m). Two centerline heat streaks are seen upstream of the lobes on side 2, while on side 1, they are less apparent since the lobes stretch to the edge of the measurement domain. The location of maximum St differs between the sides. Side 2 displays symmetric lobes and locations of maximum St, whereas side 1 shows symmetric lobes but nonsymmetric locations of maximum St. The difference in where maximum St is observed on side 1 is believed to be due to the boundary layer transitioning upstream of the view of the IR camera. It is hypothesized that this is caused by a localized roughness element located at $(x/L, y/L) = (0.09, 0.07)$, which is 23 μm in height — more than twice the height of $\overline{R_p}$ for this roughness distribution.



(a) $Re_\infty = 19.2 \times 10^6$ **/m.** **(b)** $Re_\infty = 23.0 \times 10^6$ **/m.** **(c)** $Re_\infty = 26.9 \times 10^6$ **/m.**

Fig. 11 St **contours of Side 1, as-printed roughness.**



(a) $Re_\infty = 19.2 \times 10^6$ **/m.** **(b)** $Re_\infty = 23.0 \times 10^6$ **/m.** **(c)** $Re_\infty = 26.9 \times 10^6$ **/m.**

Fig. 12 St **contours of Side 2, as-printed roughness.**

Increasing to $Re_\infty = 26.9 \times 10^6$ /m, the transition lobes exhibit upstream movement across the model from the previous condition, as previously observed in hypersonic flow [20, 21]. The shift in location of maximum heating is nominal for side 1, with $\Delta x/L \approx 0.1$, but noteworthy for side 2, with $\Delta x/L \approx 0.5$. The freestream noise environment

exhibits greater symmetry at this Re_∞, thereby leading to the equalization of transition locations. Although the location of maximum heating remains asymmetric for side 1, it is symmetric for side 2. This could possibly be attributed to the earlier mentioned roughness element.

The large-wavelength spanwise striations are prominently visible in all St distributions. Elevated heating at locations that correspond to the small wavelength roughness, which was previously identified by filtering out the striations, can only be detected after the formation of the transition lobes. These locations of elevated heating are located at $(x/L, y/L) \approx (0.7, -0.1)$ and $(x/L, y/L) \approx (0.9, 0.1)$.

Figures 13 and 14 present centerline St profiles for the as-printed roughness distributions. Superimposed on each figure is a spanwise view of the centerline roughness distribution, which extends from the nose tip to the base of the model. In addition, the centerline roughness distribution is also presented as a contour plot below the spanwise views. Laminar and Turbulent St correlations corresponding to a 7-degree half-angle cone at $M = 3.5$ and $Re_\infty = 19.2 \times 10^6$ /m are superimposed for reference [23]. The boundary-layer state is assessed using conventional knowledge of laminar, transitional, and turbulent boundary-layer heating trends. Due to the division by freestream density in Eq. 1, St decreases at a fixed streamwise location — as long as the boundary layer remains laminar or turbulent — as Re_∞ increases. The St profiles for $Re_\infty = 15.4 \times 10^6$ /m and lower indicate a laminar boundary layer, while at $Re_\infty = 19.2 \times 10^6$ /m, St begins to increase with streamwise distance, indicating a transitional boundary-layer. Additionally, St at these Re_∞ agree well with the laminar correlation for a 7-degree half-angle cone. On side 2, some profiles exhibit a subtle increase in St with increasing x/L, suggesting the boundary layer may be in a transitional state. On side 1, at $Re_\infty = 23.0 \times 10^6$ /m and $Re_\infty = 26.9 \times 10^6$ /m, the centerline boundary layer begins to transition at $x/L \approx 0.25$, where St significantly increases with x/L. This increase in St occurs immediately following a local patch of high roughness. The peak St values on side 1 occur at $x/L = 0.61$ for $Re_\infty = 23.0 \times 10^6$ /m and $x/L = 0.52$ for $Re_\infty = 26.9 \times 10^6$ /m. On side 2, St peaks at $x/L = 0.97$ for $Re_\infty = 23.0 \times 10^6$ /m, a drastic difference from side 1, and at $x/L = 0.54$ for $Re_\infty = 26.9 \times 10^6$ /m, which is four percent different from side 1.

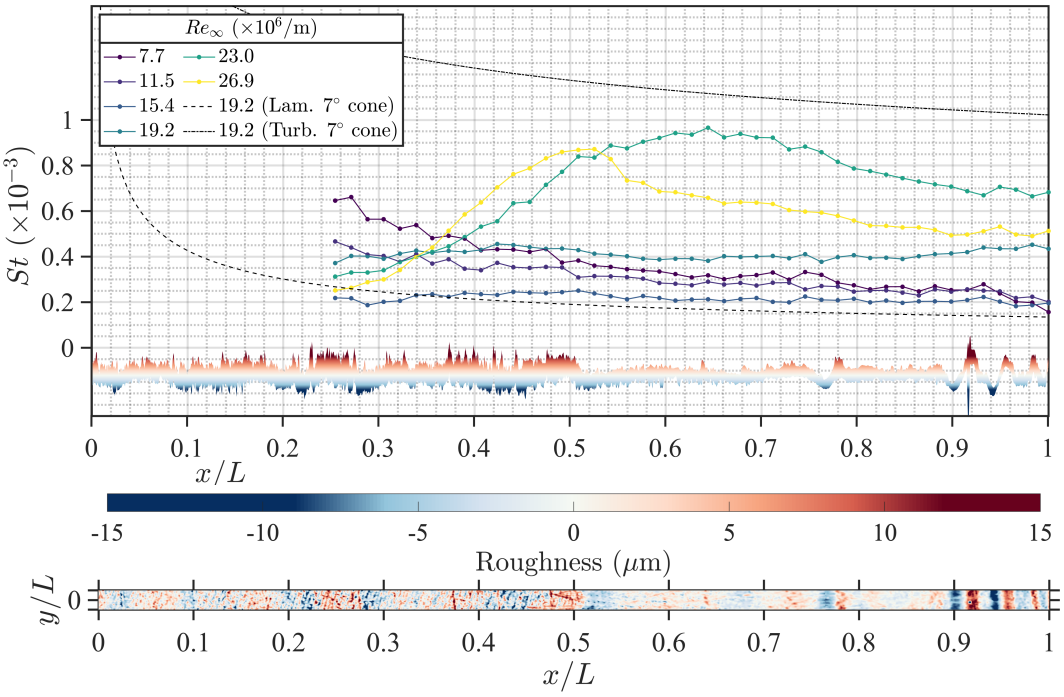


Fig. 13 Centerline St and roughness on side 1, as-printed roughness.

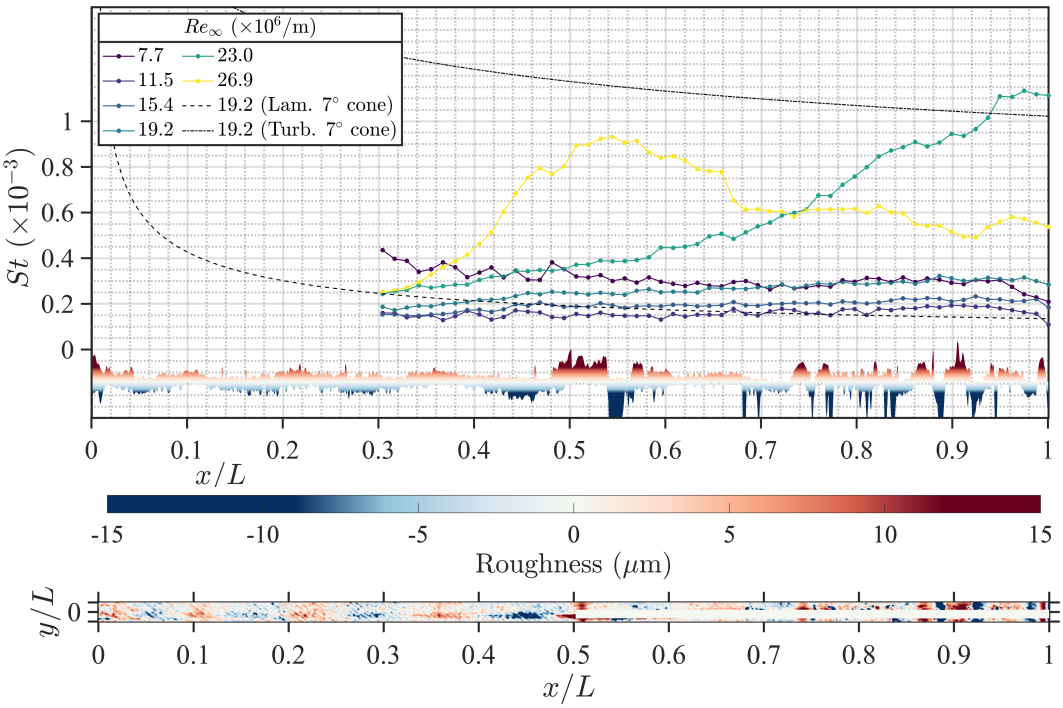


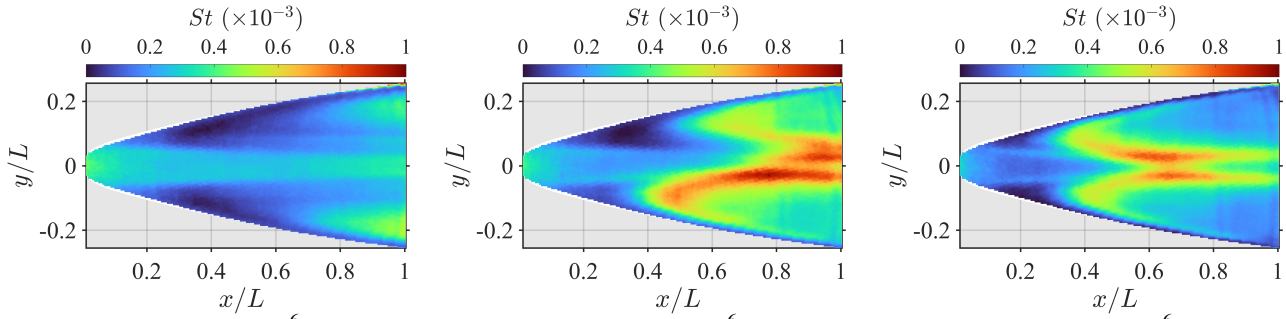
Fig. 14 Centerline St and roughness on side 2, as-printed roughness.

B. Thermography for Sanded Surfaces

Figures 15 and 16 display St contours over sides 1 and 2 of the sanded model at the same three Re_∞ previously shown for the as-printed surfaces. Note that the sanded model was rolled 90° degrees with respect to the as-printed roughness configuration, leading to an asymmetrical noise environment across each experimental surface within a range of $Re_\infty \approx 17 \times 10^6$ /m to $\approx 23 \times 10^6$ /m. At $Re_\infty = 19.2 \times 10^6$ /m, the St distribution is akin to that of the as-printed surfaces, with elevated St values near the centerline and outboard regions neighboring the base corners. Notably, a subtle change is detected in the heating distribution along the centerline, where the high temperature region becomes more narrow and concentrated between $x/L = 0.75$ and $x/L = 1.0$. Earlier computations on BOLT-1a have indicated that this concentration of flow around the center has the potential to cause the emergence of cross-flow instabilities [24, 25].

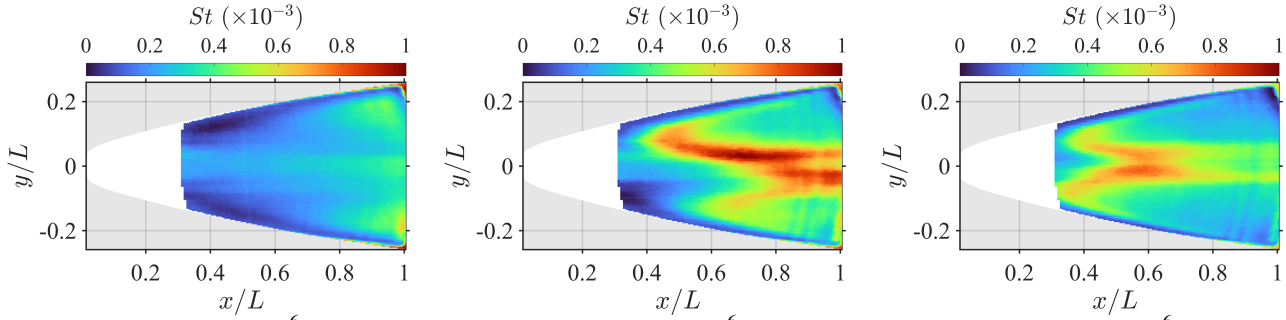
As Re_∞ reaches 23×10^6 /m, transitional lobes form, and the maximum St on each lobe remains focused near the centerline of the model. This condition significantly differs from the as-printed roughness distributions, where the lobes were symmetrical along the centerline for each corresponding surface but not symmetric with respect to each side. In contrast, for the sanded distributions, the lobes are symmetrical in relation to each surface but not concerning the centerline. This difference is attributed to the lower portion of the nozzle, inducing a higher amplitude freestream noise environment than the upper portion, causing one lobe on each side of the model to be larger than the other. At $Re_\infty = 26 \times 10^6$ /m, the freestream noise environment becomes more uniform, and the lobes exhibit the same size, shape, and location of maximum St on each corresponding side and across the centerline of the model. In Fig. 15c, hot streaks outboard of the centerline are visible. These appear to be the counterrotating vortex pair observed in previous, hypersonic BOLT-1a experiments [11, 26]. Due to a spanwise pressure gradient effect created by the nose tip, vorticity is generated within the boundary layer resulting in the formation of the vortex pair near the centerline of the model [21].

Figures 17 and 18 present centerline St profiles for the sanded model. The laminar and turbulent correlation for a 7-degree half-angle cone at $M = 3.5$ and $Re_\infty = 19.2 \times 10^6$/m is used again for reference. For $Re_\infty = 15.4 \times 10^6$/m and lower, St decreases as x/L increases until $x/L = 0.65$. At this streamwise location, the St profiles begin to increase with increasing streamwise distance, indicating the boundary layer is transitioning.



(a) $Re_\infty = 19.2 \times 10^6$ **/m.** **(b)** $Re_\infty = 23.0 \times 10^6$ **/m.** **(c)** $Re_\infty = 26.9 \times 10^6$ **/m.**

Fig. 15 *St* **contours of Side 1 sanded.**



(a) $Re_\infty = 19.2 \times 10^6$ **/m.** **(b)** $Re_\infty = 23.0 \times 10^6$ **/m.** **(c)** $Re_\infty = 26.9 \times 10^6$ **/m.**

Fig. 16 *St* **contours of Side 2 sanded.**

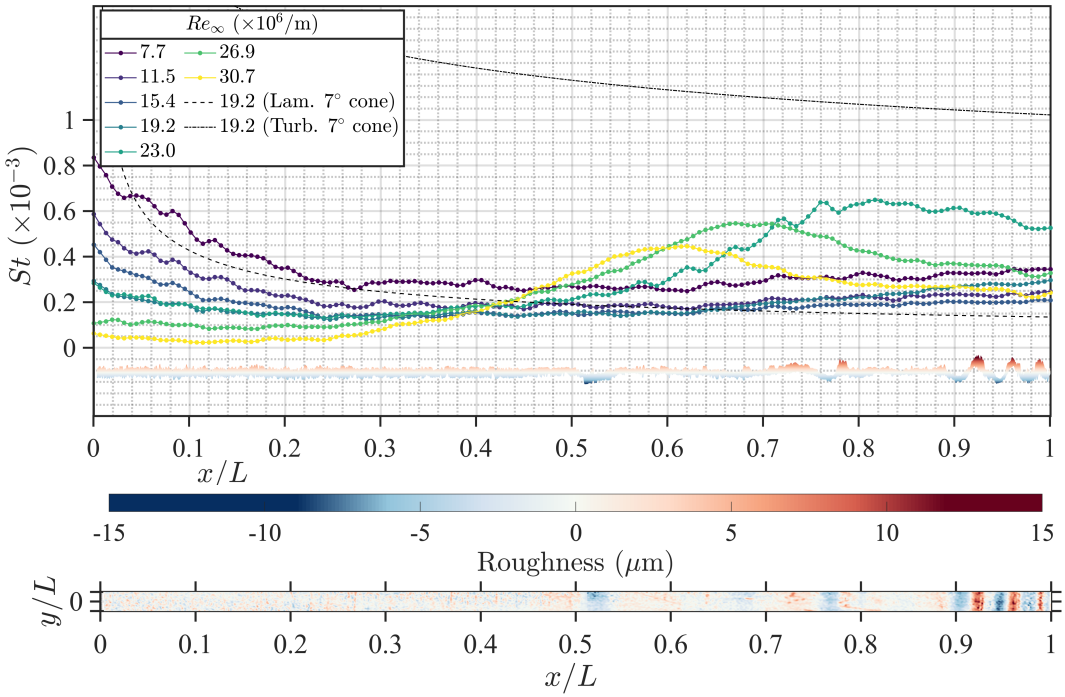


Fig. 17 Centerline *St* **and roughness on sanded side 1.**

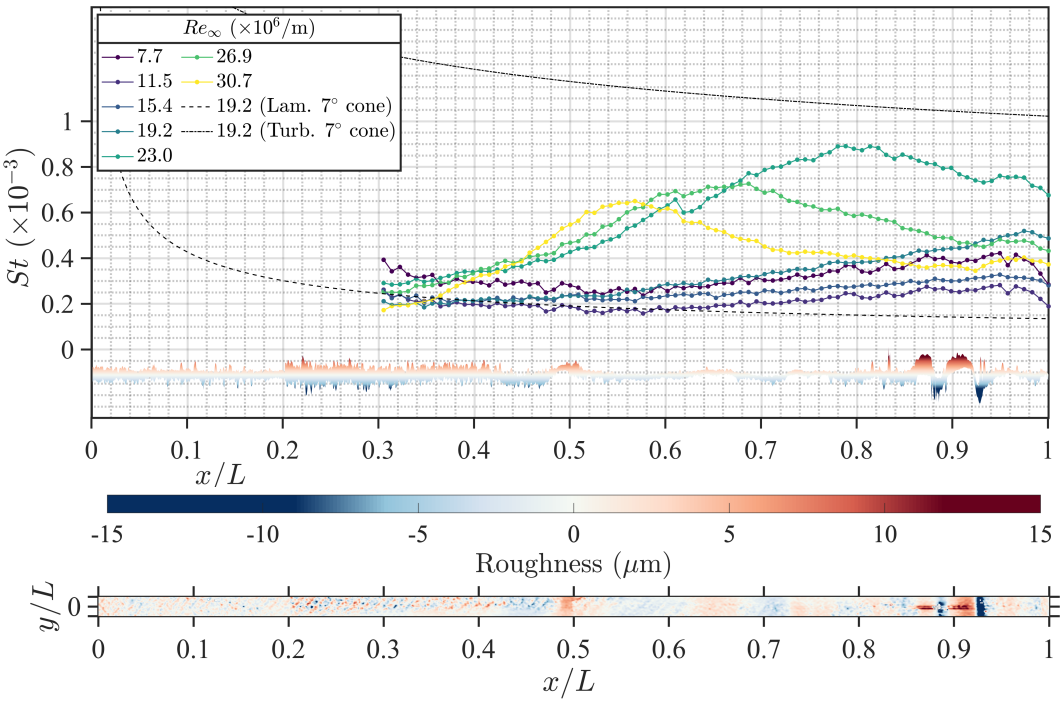


Fig. 18 Centerline *St* and roughness on sanded side 2.

Figure 19 displays boundary-layer transition location along the sanded model centerline as a function of freestream unit Reynolds number. Freestream noise level is shown as well, referring to the right axis. In this work, transition locations are taken to be where *St* commences to increase. For $Re_\infty > 15.4 \times 10^6$ /m on side 2, the transition locations are beyond the view of the IR camera, and therefore, not plotted. As Re_∞ increases, the transition location is consistently observed to shift closer to the nose tip in a quadratic manner similar to the noise level. Once Re_∞ nears $\approx 17 \times 10^6$ /m, the nozzle-wall boundary layer begins to transition and the freestream noise level increases abruptly. Once the nozzle-wall boundary layer is fully turbulent at $Re_\infty = 23.0 \times 10^6$ /m, the freestream noise level decreases causing the transition location to appear similar to that observed at $Re_\infty = 19.2 \times 10^6$ /m. Above $Re_\infty = 23 \times 10^6$ /m centerline transition resumes its upstream progression.

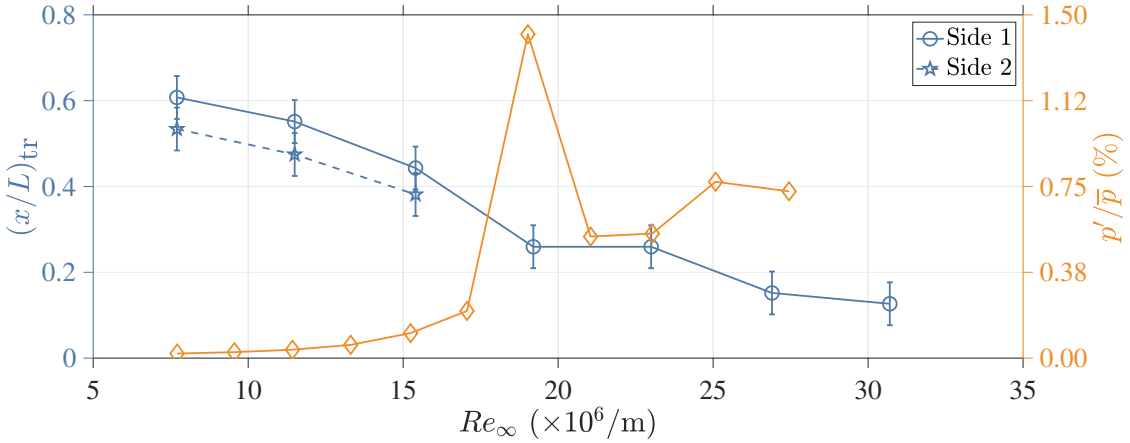


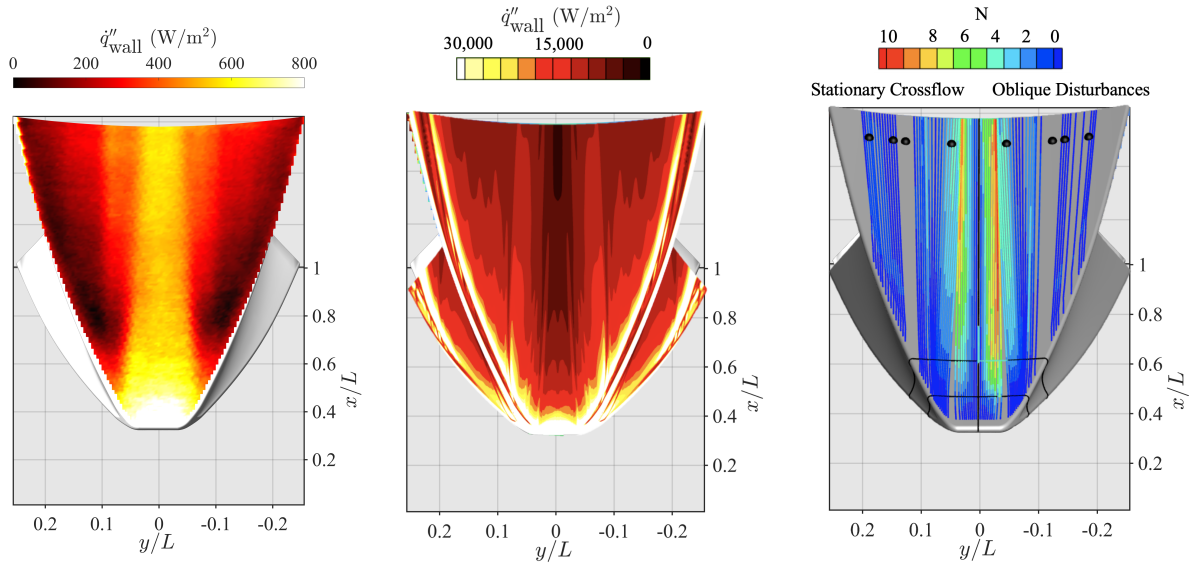
Fig. 19 Centerline transition locations for sanded surfaces.

C. Comparisons between experiment and computations

Although computations were not performed for these specific experiments, Butler et al. conducted simulations to compare with the BOLT-1a flight conditions [27]. They conducted a stability analysis with the Langley Stability and Transition Analysis Code (LASTRAC), but noted that the computations were meant as a preliminary analysis, not an authoritative assessment of the dominant instabilities. This is especially true because LASTRAC assumes spanwise homogeneity in the flow, which is not the case for this geometry. Note the simulations were performed for Re_L much larger than what was possible in these experiments.

Figure 20a displays the experimental heat-flux distribution on side 1 of the sanded model at a freestream unit Reynolds number of 15.4×10^6 /m, length Reynolds number of 1.1×10^6, Mach number of 3.5, and angle of attack of 0 degrees. At 15.4×10^6 /m in this experiment, the freestream noise levels are $p'/\overline{p} \approx 0.2\%$. Figure 20b shows the heat flux distribution on BOLT-1a as computed for flight conditions corresponding to the leeward surface with an angle of attack of -2 degrees, a freestream unit Reynolds number of 15.1×10^6/m, a Reynolds number of 17.5×10^6, and a Mach number of 2.6. The base flow solution highlights discernible heating streaks at the farthest inboard location, exhibiting a pronounced curvature towards the centerline that closely resembles the heat flux distribution observed in the experiments. As previously discussed, the bending of these streaks toward the centerline suggests amplified crossflow.

Figure 20c shows the maximum linear stability theory N factors from LASTRAC. This condition is the closest comparison to the experimental freestream unit Reynolds number and angle of attack. The largest amplification rates for both oblique disturbances and stationary crossflow are slightly off the centerline of BOLT-1a. Moreover, significant amplification is also observed for 2-D disturbances which are highly localized near the centerline. For this condition, the amplification of traveling oblique disturbances surpasses that of stationary crossflow. Butler et al. explain that the presence of multiple instability modes increases the possibility of nonlinear transition mechanisms to expedite the breakdown process. For all the various angles of attack and freestream unit Reynolds numbers computated, the greatest amplification rates were observed along a streak slightly off-centerline, as in Fig. 20c.

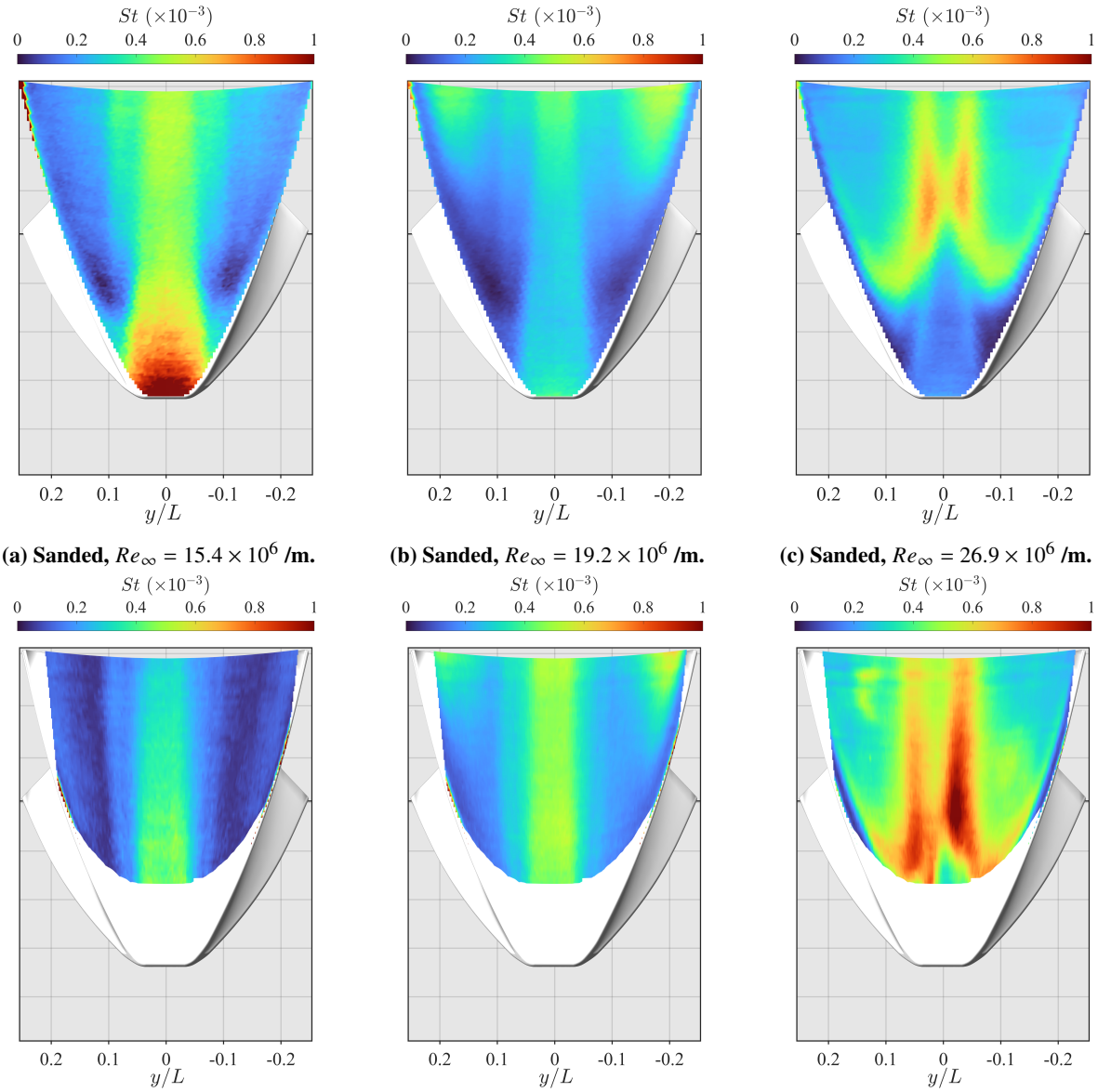


(a) Sanded $\dot{q}''$ distribution. **(b) $\dot{q}''$ Computations for descent.** **(c) N Computations for descent.**

Fig. 20 (a) Experiment: $Re_\infty = 15.4 \times 10^6$ /m, $Re_L = 1.1 \times 10^6$, $M = 3.5$, $\alpha = 0°$. (b) and (c) computations: $Re_\infty = 15.1 \times 10^6$ /m, $Re_L = 17.5 \times 10^6$, $M = 2.6$, $\alpha = -2°$ [27].

D. Effect of Surface Roughness

In Fig. 21, St distributions are compared for sanded and as-printed roughness distributions on side 1. The sanded model exhibits a centerline band of high St that gradually narrows toward the trailing edge (Figs. 21a and 21b), while the as-printed surface has a centerline band of high St that does not contract as much (Figs. 21d and 21e). At $Re = 26.9 \times 10^6$ /m (Figs. 21c and 21f), for which the freestream noise level was higher and side-lobe transition advanced, peak heating was farther upstream and less symmetric for the rougher surface.



(a) Sanded, $Re_\infty = 15.4 \times 10^6$ /m. **(b) Sanded, $Re_\infty = 19.2 \times 10^6$ /m.** **(c) Sanded, $Re_\infty = 26.9 \times 10^6$ /m.**

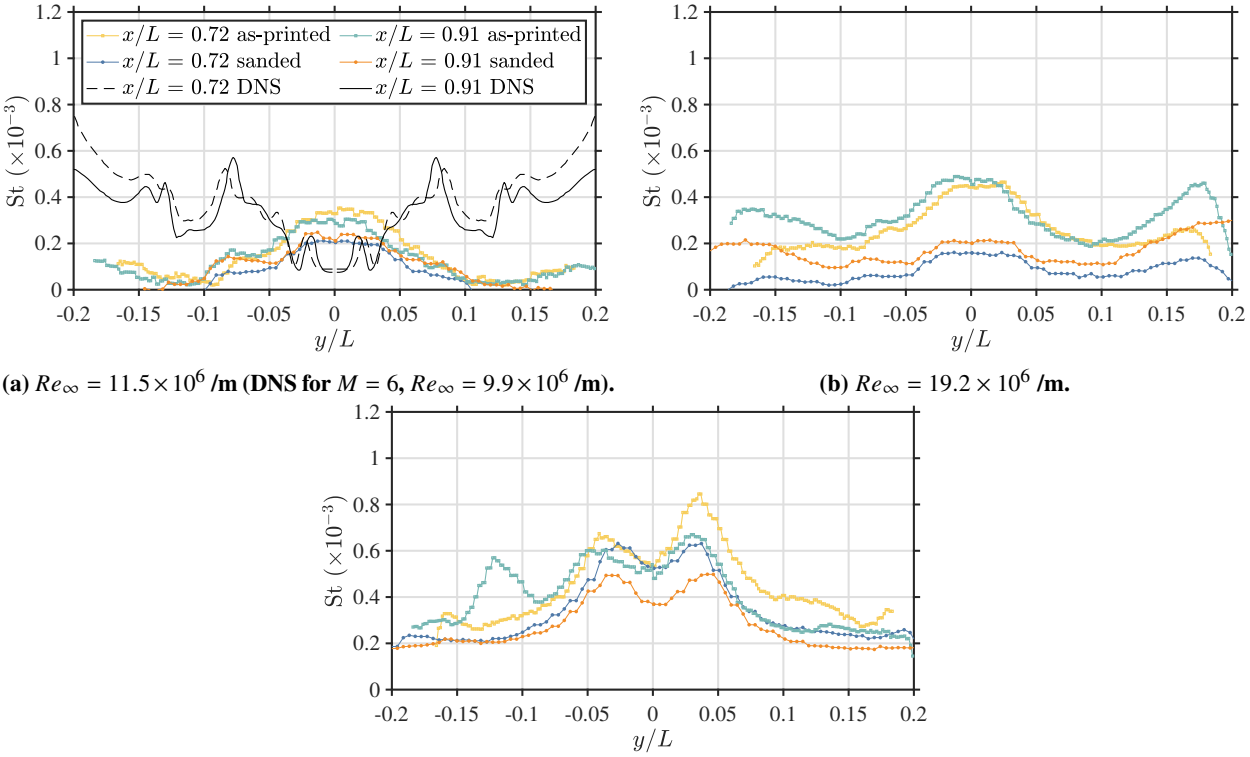
(d) As-printed, $Re_\infty = 15.4 \times 10^6$ /m. **(e) As-printed, $Re_\infty = 19.2 \times 10^6$ /m.** **(f) As-printed, $Re_\infty = 26.9 \times 10^6$ /m.**

Fig. 21 St distributions on side 1.

Differing surface heating distributions indicate the differing relative strength of the various instability mechanisms present. Of particular interest is the centerline St at $Re_\infty = 15.4 \times 10^6$/m, which is strikingly high compared to experiments at hypersonic speeds. Both simulations and experiments indicate that surface roughness enhances heat flux [21, 26], and it is plausible that roughness on the centerline contributes to the increased heat transfer. At $Re_\infty = 19.2 \times 10^6$/m, boundary-layer transition on the nozzle wall increases freestream noise, increasing St not only on the centerline but also on the outboard regions, where the crossflow instability dominates. The emergence of the transition front at a $Re_\infty = 19.2 \times 10^6$ /m resembles the three-lobed transition front observed in prior experiments on a 38.1% scale model of the HIFiRE-5 [28]. The experiment was conducted in hypersonic quiet flow ($p'/\overline{p} < 0.05\%$) and elevated heating was detected on the outer edges and at the centerline of the model. For Re_∞ from 19.2×10^6 /m (Fig. 21b) to 26.9×10^6 /m (Fig. 21c), the outboard regions progressed upstream while the centerline replicated this behavior until they eventually converged, culminating in the creation of a transition lobe.

Profiles of St at various streamwise locations are presented in Fig. 22, showing the spanwise distribution for both the as-printed and sanded side 1 at $x/L = 0.72$ and $x/L = 0.91$. To demonstrate the impact of Mach number, DNS

results from a Mach 6 simulation are also included in Fig. 22a [26]. At $Re_\infty = 11.5 \times 10^6$ /m, the sanded and as-printed distributions display similar spanwise St with slightly higher heating for the as-printed roughness. The spanwise St profiles from the DNS exhibit multiple peaks in St, corresponding to heat streaks in the streamwise direction. Notably, the two peaks near the centerline ($y/L = \pm 0.03$) correspond to vortex structures previously described. As the freestream Reynolds number is increased to $Re_\infty = 26.9 \times 10^6$ /m, the as-printed roughness causes elevated heating compared to the sanded surface. At this condition, the outboard regions exhibit elevated heating, which are more symmetric for the sanded roughness distribution. At a freestream Reynolds number of $Re_\infty = 26.9 \times 10^6$ /m, the St peaks are asymmetric for as-printed roughness, and a third peak located at $y/L = -0.13$ arises due to local roughness. In contrast, the sanded distributions exhibit symmetric heating about the centerline, indicating that roughness has a significant impact on the heating distribution.



(a) $Re_\infty = 11.5 \times 10^6$ **/m (DNS for** $M = 6$**,** $Re_\infty = 9.9 \times 10^6$ **/m).**

(b) $Re_\infty = 19.2 \times 10^6$ **/m.**

(c) $Re_\infty = 26.9 \times 10^6$ **/m.**

Fig. 22 Spanwise St **profiles.**

VII. Conclusions

Infrared thermography measurements were made on an 8.8% scale BOLT-1a model in the Probe Calibration Tunnel at NASA Langley Research Center at freestream unit Reynolds numbers from 7.7×10^6 /m to 30.7×10^6 /m, a freestream Mach number of 3.5, and nominal angle of attack of 0 degrees. The model was fabricated from polycarbonate via 3D printing. To study the impact of roughness on transition, model surfaces were scanned using a 3D optical profilometer to obtain the roughness distributions for both as-printed and sanded surfaces. Heat flux and Stanton number distributions were computed from the temperature measurements and used to identify the boundary-layer state at various freestream unit Reynolds numbers.

Heating distributions varied with Re_∞, indicating the presence of competing instability mechanisms that contribute to and persist beyond transition. One of the most interesting findings is the difference in heating observed for these experiments compared to previous hypersonic experiments. For $Re_\infty = 7.7 \times 10^6$/m to 19.2×10^6/m, relatively high heating was seen near the centerline, which differs from previous results at $M_\infty = 6$. To rule out the printed model surface roughness as the cause of the different heating distribution, repeat measurements were made after the model was sanded. This change had only a minor impact on the centerline heating.

At $Re_\infty \approx 17 \times 10^6$ /m, the nozzle-wall boundary layer begins to transition, increasing freestream noise and inducing transition. Near this condition, both the centerline and outboard regions experienced higher heating, resulting in a three-lobed transition front. Increasing Re_∞ advanced the centerline and outboard transition locations until their eventual intersection, resulting in the formation of a transition lobe on each side of the centerline. Compared to results at higher M_∞, maximum heating was concentrated along the inner, not outer region of the transition lobes. It was found that the structure of the transition lobes remained unchanged even with changes in roughness. However, the roughness did have an impact on the location of maximum heating on each lobe.

Acknowledgements

The authors express their gratitude to Dr. Louis Edelman for his assistance in fabricating the models. Jonathan Davami is supported by a University of Notre Dame Dean's Fellowship.

References

[1] Holden, M. S., and Moselle, J. R., "Theoretical and Experimental Studies of the Shock Wave-Boundary Layer Interaction on Compression Surfaces in Hypersonic Flow," *Aerospace Research Laboratories*, 1970.

[2] Babinsky, H., and Harvey, J. K., *Shock Wave-Boundary-Layer Interactions*, 1st ed., Cambridge University Press, 2011, Chap. 1, pp. 11–17. https://doi.org/10.1017/CBO9780511842757.

[3] Holden, M. S., "Shock Interaction Phenomena in Hypersonic Flows," *29th AIAA, Plasmadynamics and Lasers Conference*, 2012. https://doi.org/10.2514/6.1998-2751.

[4] Knisely, C. P., "Supersonic Unstable Modes in Hypersonic Boundary Layers with Thermochemical Nonequilibrium Effects," *UCLA Electronic Theses and Dissertations*, 2018. URL https://escholarship.org/uc/item/9cj752vt.

[5] Morkovin, M. V., "Bypass-Transition Research: Issues and Philosophy," *Fluid Mechanics and Its Applications book series (FMIA)*, Vol. 16, 1998, p. 3–30. https://doi.org/10.1007/978-94-011-1743-2_1.

[6] Herbert, T., "Secondary Instability of Boundary Layers," *Annual Reviews of Fluid Mechanics*, Vol. 20, 1988, p. 487–526. https://doi.org/https://doi.org/10.1146/annurev.fl.20.010188.002415.

[7] Perraud, J., Arnal, D., Dussillols, L., and Thivet, F., "Studies of Laminar-Turbulent Transition in Hypersonic Boundary Layers at ONERA," *SAO/NASA Astrophysics Data System (ADS)*, Vol. 426, 1998.

[8] Arnal, D., and Delery, J., "Laminar-Turbulent Transition and Shock Wave/Boundary Layer Interaction," *RTO AVT Lecture Series*, 2004. https://doi.org/https://doi.org/10.2514/8.9002.

[9] Wheaton, B., Berridge, D., Wolf, T., Araya, D., Stevens, R., McGrath, B., Kemp, B., and Adamczak, D., "Final Design of the Boundary Layer Transition (BOLT) Flight Experiment," , 2021. https://doi.org/https://doi.org/10.2514/1.A34809.

[10] Knutson, A., Thome, J., and Candler, G. V., "Numerical Simulation of Instabilities in the Boundary-Layer Transition Experiment Flowfield," *Journal of Spacecraft and Rockets*, Vol. 58, No. 1, 2021, pp. 90–99. https://doi.org/10.2514/1.A34599.

[11] Kostak, H. E., and Bowersox, R. D. W., "Preflight Ground Test Analyses of the Boundary Layer Transition (BOLT) Flight Geometry," *Journal of Spacecraft and Rockets*, Vol. 58, No. 1, 2021, pp. 67–76. https://doi.org/10.2514/1.A34858.

[12] Wheaton, B. M., Butler, C. S., McKiernan, G. R., and Berridge, D. C., "Initial Results from the BOLT Flight Experiment," , December 2021. https://doi.org/https://doi.org/10.2514/6.2022-0345.

[13] "Formlabs clear resin," https://formlabs.com/store/clear-resin/, 2022. Accessed: 2022-09-19.

[14] Franz, S., Friedrich, B., and Martin, K., "Emissivity Factor of Thermoplastic Materials for a Robot Bending Process," https://go.gale.com/ps/i.do?p=AONE&u=googlescholar&id=GALE%7CA559830205&v=2.1&it=r&sid=AONE&asid=87e928b1, 2017.

[15] Liang, E. W., Lillquist, R. D., Gallo, J. P., Poslinski, A. J., Grimson, A., and Strauss, B. R., "Predicting the Thermal Performance of an Automotive Fog Lamp Reflector," https://www.jstor.org/stable/44731304, 1997.

[16] Juliano, T. J., Adamczak, D., and Kimmel, R. L., "HIFiRE-5 Flight Test Results," *Journal of Spacecraft and Rockets*, Vol. 52, No. 3, 2015, pp. 650–663. https://doi.org/10.2514/1.A33142.

[17] Boyd, C. F., and Howell, A., "Numerical Investigation of One-Dimensional Heat-Flux Calculations," Tech. Rep. NSWCDD/TR-94/114, Dahlgren Division Naval Surface Warfare Center, Silver Spring, MD 20903-5640, October 1994.

[18] Chou, A., Kegerise, M. A., and King, R. A., "Instabilities in the Wake of a Pseudorandom Roughness on a Supersonic Flat Plate," , January 2023. https://doi.org/https://doi.org/10.2514/6.2023-0443.

[19] Gordeyev, S. V., and Thomas, F. O., "Temporal subharmonic amplitude and phase behaviour in a jet shear layer: wavelet analysis and Hamiltonian formulation," *J. Fluid Mech*, Vol. 394, 1999, pp. 205—2401. https://doi.org/https://doi.org/10.1017/S0022112099005650.

[20] Rieken, E., Berry, S., Mason, M., and Greene, F., "Aerothermodynamic Ground Tests in Support of the Boundary Layer Transition Flight Experiment," , 2021. https://doi.org/https://doi.org/10.2514/1.A34803.

[21] Kostak, H., Bowersox, D., McKiernan, G., Thome, J., Candler, G., and King, R., "Freestream Disturbance Effects on Boundary Layer Instability and Transition on the AFOSR BOLT Geometry," , 2019. https://doi.org/10.2514/6.2019-0088.

[22] Yam, C., Schneider, S. P., and Jewell, J. S., "Effects of Forward- and Backward-Facing Steps on Boundary-Layer Transition at Mach 6," , 2022. https://doi.org/https://doi.org/10.2514/6.2022-0346.

[23] Kimmel, R., and Poggie, J., "Transition on an elliptic cone at Mach 8," American Society of Mechanical Engineers ASME FEDSM97-3111, 1997.

[24] Moyes, A., Kocian, T. S., Mullen, C. D., and Reed, H. L., "Pre- Flight Boundary-Layer Stability Analysis of BOLT Geometry," , June 2018. https://doi.org/https://doi.org/10.2514/6.2018-2895.

[25] Moyes., A., and Reed, H. L., "Nonlinear Boundary-Layer Stability Analysis of BOLT and HIFiRE-5," , June 2019. https://doi.org/https://doi.org/10.2514/6.2019-2972.

[26] Thome, J., Knutson, A., and Candler, G. V., "Boundary Layer Instabilities on BoLT Subscale Geometry," , January 2019. https://doi.org/https://doi.org/10.2514/6.2019-0092.

[27] Butler, C. S., Araya, D. B., McKiernan, G. R., and Wheaton, B. M., "Supersonic Transition Measurements During the BOLT Flight Experiment Descent Phase," , June–July 2022. https://doi.org/10.2514/6.2022-4099.

[28] Juliano, T. J., Paquin, L. A., and Borg, M. P., "HIFiRE-5 Boundary-Layer Transition Measured in a Mach-6 Quiet Tunnel with Infrared Thermography," *AIAA JOURNAL*, Vol. 57, No. 1, 2019, pp. 2001–2009. https://doi.org/https://doi.org/10.2514/1.J056750.